Polyhedron 50 (2013) 532–545

Contents lists available at SciVerse ScienceDirect

Polyhedron

journal homepage: www.elsevier.com/locate/poly

Structural refinement, growth mechanism, infrared/Raman spectroscopies and photoluminescence properties of $PbMoO_4$ crystals

M.R.D. Bomio [a], L.S. Cavalcante [b,c,*], M.A.P. Almeida [d], R.L. Tranquilin [d], N.C. Batista [b], P.S. Pizani [d], M. Siu Li [e], J. Andres [f], E. Longo [c]

[a] DEMat-Universidade Federal do Rio Grande do Norte, P.O. Box 1524, 59078-970 Natal, RN, Brazil
[b] UESPI-CCN, Departamento de Química, Rua João Cabral, P.O. Box 2231, 64002-150 Teresina, PI, Brazil
[c] LIEC-Universidade Estadual Paulista, P.O. Box 355, 14801-907 Araraquara, SP, Brazil
[d] DQ-DF-UFSCar-Universidade Federal de São Carlos, P.O. Box 676, 13565-905 São Carlos, SP, Brazil
[e] IFSC-Universidade de São Paulo, P.O. Box 369, 13560-970 São Carlos, SP, Brazil
[f] Departamento de Química Física y Analítica, Universitat Jaume I, 12071 Castello, Spain

ARTICLE INFO

Article history:
Received 10 September 2012
Accepted 4 December 2012
Available online 12 December 2012

Keywords:
Clusters
Precipitation
Crystal structure
Raman
Luminescence

ABSTRACT

Lead molybdate ($PbMoO_4$) crystals were synthesized by the co-precipitation method at room temperature and then processed in a conventional hydrothermal (CH) system at low temperature (70 °C for different times). These crystals were structurally characterized by X-ray diffraction (XRD), Rietveld refinement, micro-Raman (MR) and Fourier transformed infrared (FT-IR) spectroscopies. Field emission scanning electron microscopy images were employed to observe the shape and monitor the crystal growth process. The optical properties were investigated by ultraviolet–visible (UV–Vis) absorption and photoluminescence (PL) measurements. XRD patterns and MR spectra indicate that these crystals have a scheelite-type tetragonal structure. Rietveld refinement data possibilities the evaluation of distortions in the tetrahedral $[MoO_4]$ clusters. MR and FT-IR spectra exhibited a high mode $\nu_1(A_g)$ ascribed to symmetric stretching vibrations as well as a large absorption band with two modes $\nu_3(E_u$ and $A_u)$ related to anti-symmetric stretching vibrations in $[MoO_4]$ clusters. Growth mechanisms were proposed to explain the stages involved for the formation of octahedron-like $PbMoO_4$ crystals. UV–Vis absorption spectra indicate a reduction in optical band gap with an increase in the CH processing time. PL properties of $PbMoO_4$ crystals have been elucidated using a model based on distortions of tetrahedral $[MoO_4]$ clusters due to medium-range intrinsic defects and intermediary energy levels (deep and shallow holes) within the band gap.

1. Introduction

Molybdates with a scheelite-type tetragonal structure have a general formula ($AMoO_4$) are composed of larger divalent cations (A = Ca, Sr, Ba, and Pb; ionic radius > 0.99 Å). These materials have a space group ($I4_1/a$), point-group symmetry (C_{4h}^6) and four molecular formulas per unit cell ($Z = 4$) [1–6]. In the crystal lattice, each molybdenum (Mo) atom is coordinated by four oxygen (O) atoms which results in $[MoO_4]$ clusters while the A atoms are connected by eight O atoms to form $[AO_8]$ clusters [7,8].

Previously, structural parameters of $PbMoO_4$ (PMO) crystals have been obtained by the Rietveld method [9–12]. This structural refinement method presents several advantages over conventional quantitative analysis methods. As the method uses a whole pattern-fitting algorithm, all lines for each phase are explicitly considered, and even severely overlapped lines are usually not a problem. Thus, it is not necessary to decompose patterns into separate Bragg peaks, as is often the case for traditional methods. The use of all reflections in a pattern rather than just the strongest ones minimizes both uncertainty in the derived weight fractions and the effects of preferred orientation, primary extinction and non-linear detection systems [13]. In recent paper [14], our group applied this method to investigate structural parameters (intrinsic defects by octahedral tilt angle) in $CaTiO_3$ powders to explain their optical properties. In another study, Li et al. [15] employed this method to analyze the effect of $CaWO_4$ crystal size reduction with an increase in the unit cell volume and c/a (lattice parameters) ratio. As a consequence of this phenomenon, a decrease in photoluminescence (PL) properties of these nanocrystals was observed.

Research involving the crystal growth (solids immersed in liquids) and/or formation of crystals precipitated from solutions mainly involve the nucleation and growth [16]. Therefore, the formation of crystals with different shapes and sizes depends on the average concentration of the solution (unsaturated, saturated

* Corresponding author at: UESPI-CCN, Departamento de Química, Rua João Cabral, P.O. Box 2231, 64002-150 Teresina, PI, Brazil.
E-mail address: laeciosc@bol.com.br (L.S. Cavalcante).

0277-5387/$ - see front matter © 2012 Elsevier Ltd. All rights reserved.
http://dx.doi.org/10.1016/j.poly.2012.12.001

and supersaturated) [17]. Nanocrystals can be formed starting with unsaturated solutions from colloidal systems. The first clusters are formed in a solution saturated at equilibrium [18]. Nucleation process occurs when crystals precipitate in saturated solutions. The formation and accumulation of stable nuclei [19] occur when supersaturation is sufficiently high to overcome the nucleation energy barrier. In supersaturated solutions, crystal precipitates are already formed at the completion of the nucleation. In this system, crystals continue to grow; different types of growth mechanisms can be verified depending on the crystal growth process [20,21].

For PMO crystals, two types of growth mechanism have been reported in the literature: predominant Ostwald ripening (OR) and/or oriented attachment (OA) [22–24]. In the OR mechanism, small crystals are dissolved and deposited on larger crystals. This thermodynamically-driven spontaneous process occurs because the larger crystals are more energetically favored than smaller crystals. In OR mechanism, atoms on the crystal surface are energetically less stable than atoms in the interior [25,26]. On the other hand, the OA mechanism is a process where adjacent crystals are self-assembled by sharing a common crystallographic orientation and docking of these crystals at the same planar interface [27–30].

Moreover, molybdates have electronic properties in several fields such as PL, photocatalytic, electrochemical, microwave dielectric, scintillator and red phosphors [31–46]. As an important member of scheelites, PMO crystals have been widely applied as scintillators, acoustooptic modulators/detectors, etc. [47–51].

Therefore, in this paper, we report the structural refinement and optical properties of PMO crystals synthesized by co-precipitation (CP) method at room temperature and then processed in a conventional hydrothermal (CH) system at 70 °C for different times. Furthermore, these crystals were structurally characterized by X-ray diffraction (XRD), micro-Raman (MR) and Fourier transformed infrared (FT-IR) spectroscopies. Field emission scanning electron microscopy (FE-SEM) was employed to verify the shape and monitor the growth process of these crystals with CH processing time. Finally, the intense visible PL emission of these crystals were explained with basis in presence of intermediary level energy, shallow/deep defects at medium range, and the crystal size/crystallographic orientation.

2. Experimental procedure

2.1. Co-precipitation and hydrothermal conventional processing of $PbMoO_4$ crystals

PMO crystals were obtained by CP and CH methods in the absence of surfactants. The typical synthesis procedure is described as follows: 0.005 mol of molybdic acid (H_2MoO_4) (85% purity, Synth) and 0.005 mol of lead nitrate [$Pb(NO_3)_2$] (99.5% purity, Merck) were dissolved in 75 mL of deionized water. Then 5 mL of ammonium hydroxide (NH_4OH) (30% in NH_3, Synth) was added to the solution until the pH value reached 10. These suspensions were stirred for 10 min by ultrasound at room temperature. With this procedure, PMO crystals were obtained by the CP method (later called precipitated crystals). In a precipitation reaction, Pb^{2+} cations are electron pair acceptors (Lewis acids) while MoO_4^{2-} anions are electron pair donors (Lewis bases). The chemical reaction between these two species in solutions results in the formation of PMO crystals as shown in the equations below:

$$H_2MoO_{4(s)} + Pb(NO_3)_{2(s)} \xrightarrow{H_2O} 2H^+_{(aq)} + 2NO^-_{3(aq)} + Pb^{2+}_{(aq)} + MoO^{2-}_{4(aq)} \quad (1)$$

$$Pb^{2+}_{(aq)} + MoO^{2-}_{4(aq)} \rightarrow PbMoO_{4(s)} \downarrow \quad (2)$$

These suspensions were transferred into a stainless steel autoclave (lined with quartz glass) which was sealed and processed at 70 °C for different times (2, 4, 8, and 10 min) using a heating rate fixed at 2 °C/min and a pressure of 233.7 mmHg (NANOX TECNOLOGY S/A, Nanox Hidrocell H100, Brazil) [52] (see Support Information, Fig. SI-1). After CH processing, the autoclave was cooled at room temperature. The resulting suspensions were washed several times with deionized water to neutralize the pH solution (≈7), and the white precipitates were dried with acetone and finally collected for characterizations.

2.2. Characterizations of $PbMoO_4$ crystals

After CP at room temperature and CH processing at 70 °C for different times, these PMO crystals were structurally characterized by XRD using a Rigaku-DMax/2500PC (Japan) with Cu Kα radiation (λ = 1.5406 Å) in the 2θ range from 10° to 75° with a scanning rate of 0.02°/s and a total exposure time of 15 min. Moreover, Rietveld routine was performed in the 2θ range from 10° to 110°, using an angular step of 0.02°/s and exposure total time of 90 min. MR measurements were recorded using a T-64000 spectrometer (Jobin-Yvon, France) triple monochromator coupled to a CCD detector with a 488 nm wavelength of an argon ion laser. Its maximum output power was kept at 10 mW with the use of a lens (100 μm) to prevent sample overheating. FT-IR spectra were taken in the range from 200 to 1000 cm^{-1} using KBr pellets as a reference using a Bomem–Michelson spectrophotometer in transmittance mode, model MB-102. The morphologies were investigated using FE-SEM (Carl Zeiss, model Supra 35-VP, Germany) operated at 15 kV. UV–Vis spectra were taken using a Varian spectrophotometer, model Cary 5G (USA) in diffuse reflection mode with MgO as a standard. PL measurements at room temperature were performed using a Monospec 27 monochromator (Thermal Jarrel Ash, USA) coupled to a R446 photomultiplier (Hamamatsu Photonics, Japan). A krypton ion laser (Coherent Innova 90K, USA) (λ = 350 nm) was used as an excitation source; its maximum output power was kept at 500 mW with maximum power on the sample after passing through an optical chopper of 40 mW.

3. Results and discussion

3.1. XRD patterns analyses

Fig. SI-2 (Support Information) illustrates XRD patterns of PMO crystals obtained by the CP method and processed at 70 °C for different times (from 2 to 10 min) in a CH system.

Fig. SI-2 (Support Information) shows the XRD patterns of PMO crystals which can be indexed to a scheelite-type tetragonal structure with a space group $I4_1/a$ and is in agreement with the respective Inorganic Crystal Structure Database (ICSD) No. 26784 [53]. Diffraction peaks related to secondary phases were not detected which indicates that a monophasic system was obtained. Also, these peaks are intense and well defined which suggests a considerable degree of structural order at long-range [54]. Lattice parameters and unit cell volume were calculated using the MAUD program version 2.26 for material analysis by diffraction in a Windows-XP platform [55–59]. This program employs a general diffraction/reflectivity analysis based on the Rietveld method [60]. The values found for lattice parameters and cell volume are shown in Support Information, Fig. SI-3 and are presented in Table 1.

The results obtained from the Rietveld refinement of lattice parameters and unit cell of PMO crystals are very close to the results reported in the literature [61–64] with the respective ICSD No. 26784 [53]. However, small variations in these values can be due to different types of synthesis methods and the experimental

Table 1
Comparative results between the lattice parameters, unit cell volume, b/c and c/a ratios for PMO crystals obtained in this study with those reported literature values by different synthesis methods.

M	T (°C)	t (min)	Lattice $a = b$	Parameters c (Å)	b/c ratio	c/a ratio	V (Å^3)	Ref.
CZ	1200	1440	5.4351(3)	12.1056(8)	0.4489	2.227	357.60(3)	[61]
CH	160	1200	5.433	12.11	0.4486	2.229	357.456	[62]
SC	–	60	5.4233	12.1253	0.4472	2.2357	356.631	[63]
MI	–	20	5.407	12.0388	0.4491	2.2265	351.962	[64]
CP	25	10	5.423(2)	12.103(8)	0.4881	2.2319	355.99	[✠]
CH	70	2	5.432(5)	12.124(0)	0.4481	2.2318	357.80	[✠]
CH	70	4	5.435(6)	12.130(8)	0.4481	2.2317	358.41	[✠]
CH	70	8	5.424(3)	12.114(7)	0.4477	2.2334	356.45	[✠]
CH	70	10	5.422(5)	12.092(5)	0.4484	2.2301	355.56	[✠]
ICSD	N. 26784	–	5.43121(6)	12.1065(4)	0.4486	2.2290	357.120	[53]

M = method; T = temperature; t = processing time; a, b, c = lattice parameters; V = unit cell volume; $\alpha = \beta = \gamma$ angles = 90°; Ref. = references; CZ = Czochralski; CH = conventional hydrothermal; SC = sonochemical; MI = microwave irradiation; CP = coprecipitation and [✠] = this work.

conditions employed such as temperature, time, heating rate, atmosphere, ultrasound, microwave irradiation (see Support Information, Fig. SI-3 and Table 1) which leads to different levels of structural organizations at long-range in the PMO lattice.

3.2. Rietveld refinement data analyses

Fig. 1(a)–(e) shows the structural refinement plot for PMO crystals synthesized by the CP method and processed at 70 °C for different times (from 2 to 10 min) in a CH system.

The results obtained by the Rietveld refinement method indicate good agreement between the observed XRD patterns and theoretical results. Moreover, the difference between the experimental XRD profile patterns observed and theoretical calculated data display small differences close to zero in the scale of intensity as illustrated by a line ($Y_{observed} - Y_{calculated}$). The 2D XRD multiplot (residuals) are indicated by colors (Fig. 1(a)–(e)). In this study, we initially applied the Rietveld method or full pattern analysis for the structural refinement of PMO crystals. The Rietveld method is a least squares refinement procedure where the experimental step-scanned values are adapted to calculated values. The profiles are considered to be known, and a model for a crystal structure is available [65]. The observed experimental XRD pattern profiles of PMO crystals were refined with a theoretical line profile known as a Crystallographic Information File (CIF) [66] which is related to the respective ICSD No. 26784 [53].

Rietveld refinements performed with the MAUD program [55] employed the Rietveld texture and stress analysis [57]. The optimized parameters were: scale factor, background with exponential shift, exponential thermal shift, polynomial coefficients, basic phase, microstructure, crystal structure, microstrain, structure solution model, structure factor extractor, shift lattice constants, profile half-width parameters (u, v, w), texture, lattice parameters (a, b, c) and site occupancy factors (Wyckoff) and were used to obtain a structural refinement with better quality and reliability [67,68]. All Rietveld refinements for PMO crystals were performed based on a scheelite-type tetragonal structure and space group ($I4_1/a$) with a better approximation and indexing with a CIF file as indicated in ICSD No. 26784 [53]. According to the literature [65], the quality of data from structural refinement is generally checked by R-values (R_{wnb}, R_b, R_{exp}, R_w and σ), and therefore the numbers obtained for R-values and σ can be easy reported.

The quality of the structural refinement data is acceptable when the R_w is <10% for a medium complex phase. For a high complex phase (monoclinic to triclinic), a value of $R_w < 15\%$ and for a highly symmetrical material or a compound (cubic) with few peaks, a value of $R_w < 8\%$ is acceptable. It is also important to verify σ values. A good refinement gives σ values lower than 2. However, in experimental XRD pattern profiles with very high intensities and low noise patterns, it is difficult to reach a value of $\sigma = 2$ for all PMO crystals. The results obtained from the Rietveld refinement are presented in Table 2.

In this table, the fitting parameters (R_{wnb}, R_b, R_{exp}, R_w and σ) indicate good agreement between refined and observed XRD patterns of PMO crystals with a tetragonal structure. Table 2 shows some variations in atomic positions of O atoms while Pb and Mo atoms have fixed atomic positions. These results indicate that O atoms are very disturbed into lattice. Based in results we can proposed the presence of distortions in the [MoO_4] clusters in the lattice. Moreover, Rietveld refinement results obtained in this study are in good agreement with results reported in the literature [69–71].

3.3. Representations of $PbMoO_4$ unit cells from the Rietveld refinement data

Fig. 2(a)–(e) displays schematic representations for tetragonal PMO unit cells calculated from Rietveld refinement data.

These unit cells were modeled using the Diamond Crystal and Molecular Structure Visualization (Version 3.2g for Windows) program [72] with lattice parameters and atomic positions obtained from Rietveld refinement data (see Tables 1 and 2). PMO crystals belong to scheelite-type tetragonal structure (space group $I4_1/a$, No. 88 in the international tables of crystallography and point-group symmetry (C_{4h}^6) [73]. Fig. 2(a)–(e) illustrates that bonds between O–Mo–O and O–Pb–O atoms were projected out of the unit cell. In these unit cells, the Mo atoms are coordinated to four O atoms which form [MoO_4] clusters with a tetrahedral configuration and tetrahedron polyhedra (4 vertices, 4 faces and 6 edges) [74]. These [MoO_4] clusters are slightly distorted in the lattice and exhibit a particular characteristic related to differences in the O–Mo–O bond angles (Fig. 2(a)–(e)). This behavior can be due to different synthesis methods (CP and CH) employed in the preparation of these crystals. On the other hand, the Pb atoms are bonded to eight O atoms which results in deltahedral [PbO_8] clusters and snub disphenoide-type polyhedra (8 vertices, 12 faces and 18 edges) [75]. Moreover, we note possible distortions in [PbO_8] clusters with different angles between the O–Pb–O atoms. However, these distortions are much more complex to analyzed and explained in details (see Support Information, Fig. SI-4(a)–(e)).

3.4. Micro-Raman and infrared spectroscopies analyses

According to group theory calculations, molybdates with a scheelite-type tetragonal structure exhibit 26 different (Raman and infrared) vibrational modes which are represented by Eq. (3) [76–78]:

$$\Gamma_{(Raman+Infrared)} = 3A_g + 5A_u + 5B_g + 3B_u + 5E_g + 5E_u \quad (3)$$

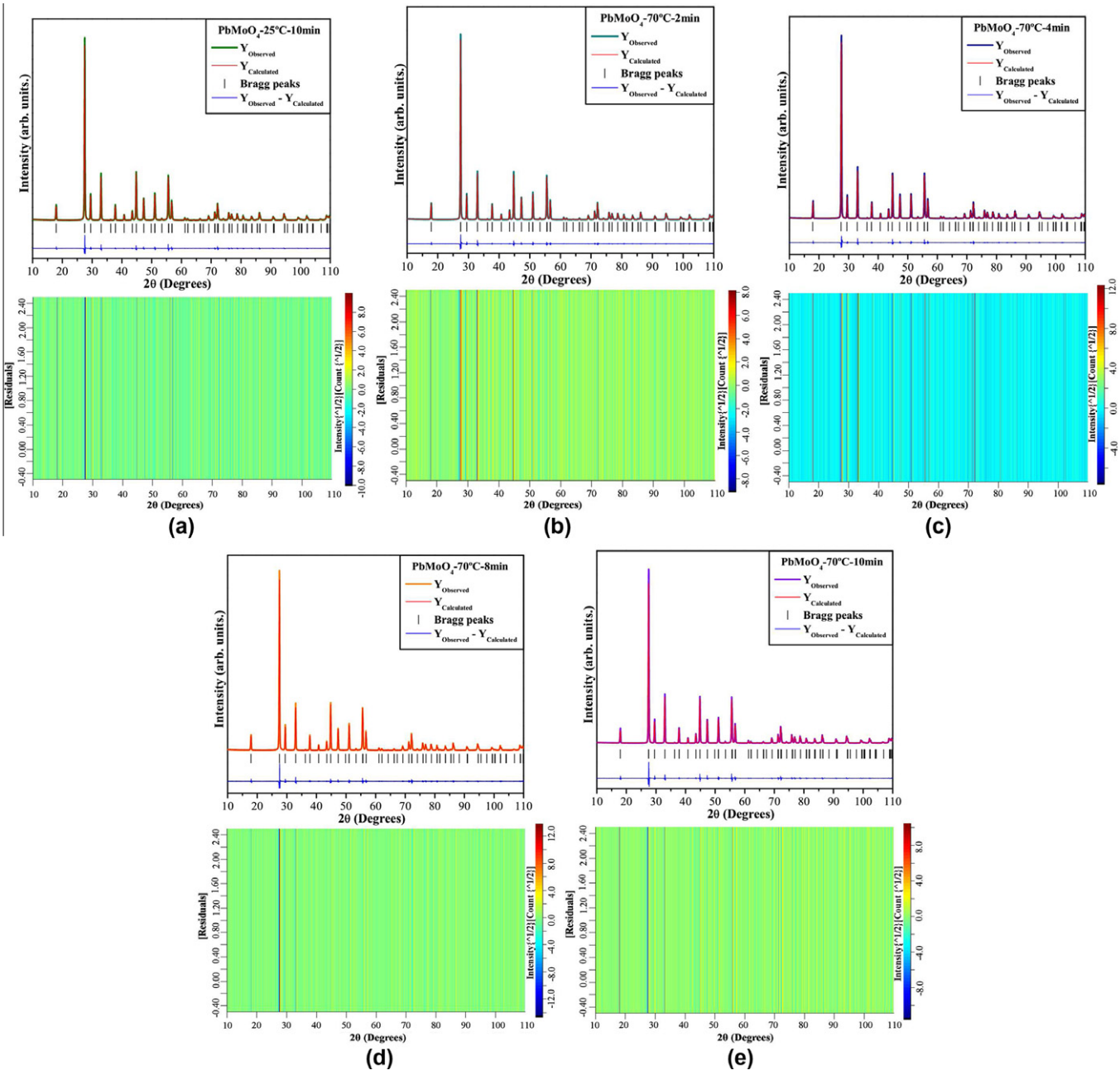

Fig. 1. Rietveld refinement plot and 2D multiplot (residuals) of PMO crystals prepared by the: (a) CP method and processed at 70 °C for different times: (b) 2 min, (c) 4 min, (d) 8 min and (e) 10 min in a CH system.

where A_g, B_g, and E_g are Raman-active vibrational modes, and A and B modes are non-degenerate while E modes are doubly degenerate. The subscripts (g) and (u) indicate the pairs under inversion in centrosymmetric PMO crystals. A_g, B_g, and E_g Raman modes are the result of the motion of clusters in the crystal lattice. Therefore, 13 Raman-active vibrational modes of the PMO crystals are anticipated as indicated in Eq. (4) [79,80]:

$$\Gamma_{(Raman)} = 3A_g + 5B_g + 5E_g \quad (4)$$

According to Basiev et al. [81,82], the vibrational modes observed in Raman spectra for the molybdates are classified into two groups (external and internal modes). The external vibration modes are related to lattice phonons which correspond to [PbO_8] cluster motion with a symmetry point (D_{2d}) in rigid cell units. Vibrational internal modes are related to [MoO_4] cluster vibration in the lattice (assuming the center of mass is in a stationary state). Isolated [MoO_4] tetrahedrons have a cubic symmetry point (T_d) [81], and their vibrations are composed of four internal modes [$v_1(A_1)$, $v_2(E_1)$, $v_3(F_2)$ and $v_4(F_2)$], one free rotation mode [$v_{f.r.}(F_1)$] and one translational mode [(F_2)]. On the other hand, when tetrahedral [MoO_4] clusters are located in the scheelite lattice, their point symmetry is reduced to S_4 [81].

As illustrated in Eq. (4), after excluding 13 Raman vibrational modes, we have 13 infrared vibrational modes as demonstrated by Eq. (5) [83]:

$$\Gamma_{(Infrared)} = 5A_u + 3B_u + 5E_u \quad (5)$$

However, among the 13 infrared vibrational modes, a number are not observable; e.g, $1A_u$ and $1E_u$ infrared modes correspond to the zero wavenumber of acoustic modes at the center of the

Table 2
Atomic coordinates employed to model PMO unit cells and (α and β) angles between chemical bonds O–Mo–O in [MoO_4] clusters.

Atoms	Wyckoff	x	y	z
♣				
Lead	4b	0	0.25	0.625
Molybdenum	4a	0	0.25	0.125
Oxygen	16f	0.17127	0.12103	0.04576
R_w = 6.05%; R_{wnb} = 6.46%; R_b = 4.76%; R_{exp} = 3.33% and σ = 1.82				
■				
Lead	4b	0	0.25	0.625
Molybdenum	4a	0	0.25	0.125
Oxygen	16f	0.20934	0.13244	0.04959
R_w = 6.03%; R_{wnb} = 8.57%; R_b = 4.59%; R_{exp} = 3.3% and σ = 1.83				
★				
Lead	4b	0	0.25	0.625
Molybdenum	4a	0	0.25	0.125
Oxygen	16f	0.20841	0.13252	0.05021
R_w = 6.08%; R_{wnb} = 9.77%; R_b = 4.50%; R_{exp} = 3.28% and σ = 1.85				
◆				
Lead	4b	0	0.25	0.625
Molybdenum	4a	0	0.25	0.125
Oxygen	16f	0.21027	0.14685	0.05176
R_w = 7.25%; R_{wnb} = 8.54%; R_b = 5.45%; R_{exp} = 3.38% and σ = 2.14				
•				
Lead	4b	0	0.25	0.625
Molybdenum	4a	0	0.25	0.125
Oxygen	16f	0.21454	0.14973	0.05458
R_w = 8.42%; R_{wnb} = 10.57%; R_b = 6.58%; R_{exp} = 4.16% and σ = 2.02				

♣ = PMO-CP-25 °C-10 min; ■ = PMO-CH-70 °C-2 min; ★ = PMO-CH-70 °C-4 min; ◆ = PMO-CH-70 °C-8 min and • = PMO-CH-70 °C-10 min.

Brillouin zone, $3B_u$ infrared modes are forbidden infrared modes, and the balance are optical modes. Therefore, only eight infrared-active vibrational modes remain which are $4A_u$ modes that are perpendicular to the *c*-axis and $4E_u$ modes with the electric vector parallel to the *c*-axis as indicated in Eq. (6) [84,85]:

$$\Gamma_{(Infrared)} = 4A_u + 4E_u \quad (6)$$

Fig. 3 illustrates MR spectra of PMO crystals obtained by the CP method and processed at 70 °C for different times (from 2 to 10 min) in a CH system.

In Fig. 3, only 10 of the 13 Raman active modes can be detected; no ($1A_g$ and $2E_g$) Raman vibrational modes were observed. We believe that this behavior can be due to the low intensity of the modes, although Fig. 3 shows a MR spectrum with well defined and sharp peaks that indicate characteristics of materials with structural order at short-range [86]. In addition, other factors may produce these characteristics such as preparation method, low temperature of synthesis/processing, geometry and/or crystal size. In particular, the PMO crystal lattice is characterized by bonds with a covalent/ionic character between the O–Pb–O and O–Mo–O, respectively. Thus, we expect that among the molybdates $AMoO_4$ (*A* = Ba, Sr, Ca, and Pb) [87–90] the PMO crystal bonds have a covalent nature predominantly in the lattice due to [PbO_8] clusters while the other crystals have lattices with an ionic nature due to [CaO_8], [SrO_8] and [BaO_8] clusters with major differences in electronegativities between the alkaline-earth metals and oxygen atoms. The inset of Fig. 3 depicts [MoO_4] clusters with symmetric stretching vibrations between O–Mo–O bonds. The positions of each Raman-active mode are listed in Table 3 and are compared with Raman-active modes in the literature [91–94].

An analysis of the results presented in this table indicate that the relative positions of all Raman-active modes of PMO crystals reported here are in reasonable agreement with others papers reported in the literature [91–94]. Slight shifts in these positions can be correlated to the degree of structural order and/or distortion of the PMO lattice induced by synthesis methods. These conditions produce different levels of distortions on [MoO_4] clusters (Fig. 2(a)–(e)). Also, it is possible that the degree of interaction between O–Pb–O–Mo–O bonds and/or variations in the O–Pb–O–Mo–O bond lengths induce shifts in the Raman peak positions.

Fig. 4 illustrates FT-IR spectra of PMO crystals which were obtained by the CP method and processed at 70 °C for different times (from 2 to 10 min) in a CH system.

As previously described, molybdates with a scheelite-type tetragonal structure have up to eight stretching and/or bending vibrational modes in infrared spectra [86,95]. In our case, it was possible to identify no more than six modes ($3A_u$ and $3E_u$) which were found in specific positions in the spectra (Fig. 4). First, there are strong absorption bands with two modes located at 749/756 and 864/851 cm^{-1} for all PMO crystals precipitated and processed in a CH system for different times, respectively. These two bands are related to v_3($1E_u$ and $1A_u$) internal modes originating from anti-symmetric stretching vibrations in [MoO_4] clusters [86,91]. Similarly, two other v_4($1A_u$ and $1E_u$) modes are assigned which are linked to the anti-symmetric bending of bonds in [MoO_4] clusters. These modes are located at around 372/374 cm^{-1} for PMO crystals precipitated and processed in a CH system for different times, respectively. Finally, the other two absorption bands located at 304/306 cm^{-1} and 264/266 cm^{-1} are ascribed to the v_2($1A_u$ mode) and the ($1E_u$ mode). These modes refer to the symmetric bending of O–Mo–O bonds in [MoO_4] clusters. In Fig. 4, the vertical lines are used as guides. Only precipitated PMO crystals have infrared bands at different positions in relation to other crystals. All PMO crystals processed at 70 °C for different times did not produce a significative shift in the positions of the six infrared modes. This behavior can be related to the presence of crystals with very similar O–Mo–O bonds (Fig. 2(a)–(e) and Table 2). Moreover, PMO crystals processed in a CH system for different times have a similar energy coupling and bonding strength between the O–Mo–O in [MoO_4] clusters and/or O–Pb–O in [PbO_8] clusters, respectively.

Table 4 compares relative positions between infrared-active modes of PMO crystals obtained in this study with those reported literature results [91,95,96].

An analysis of the results in Table 4 shows a shift in the values of v_3(E_u and A_u) modes. We believe that this behavior can possibly be related to different interaction strengths and stretching or bond angles between O–Mo–O bonds due to distortions in tetrahedral [MoO_4] clusters in the lattice.

3.5. FE-SEM analyses of $PbMoO_4$ crystals

Fig. 5(a)–(j) shows the FE-SEM images of PMO crystals obtained by the CP method and processed at 70 °C for different times (from 2 to 10 min) in a CH system.

FE-SEM images were employed to monitor the evolution shape and growth process of PMO crystals with an increase in CH processing time. Fig. 5(a) and (b) shows small octahedron-like PMO crystals formed at room temperature by the CP method. The crystals formed by this method have surface defects on their faces which are probably caused by rapid hydrolysis during the addition of NH_4OH into the solution [7]. In addition, this behavior can be related to the formation of a supersaturated solution due to a high concentration of chemical acid/salts dissolved in the aqueous medium (75 mL) [97]. PMO crystals with these shape characteristics can be classified as primary agglomerates composed of small crystals (crystallites) a few nanometers in size. Moreover, these morphological characteristics suggest that the growth rate of each crystal face is usually non-linearly proportional to the supersaturation of the solution [31]. Processing performed at 70 °C for 2 min (Fig. 5(c) and (d)) produced a crystal growth of sharper octahedrons with faces along different crystallographic planes. However, it was verified that the agglomerate nature still

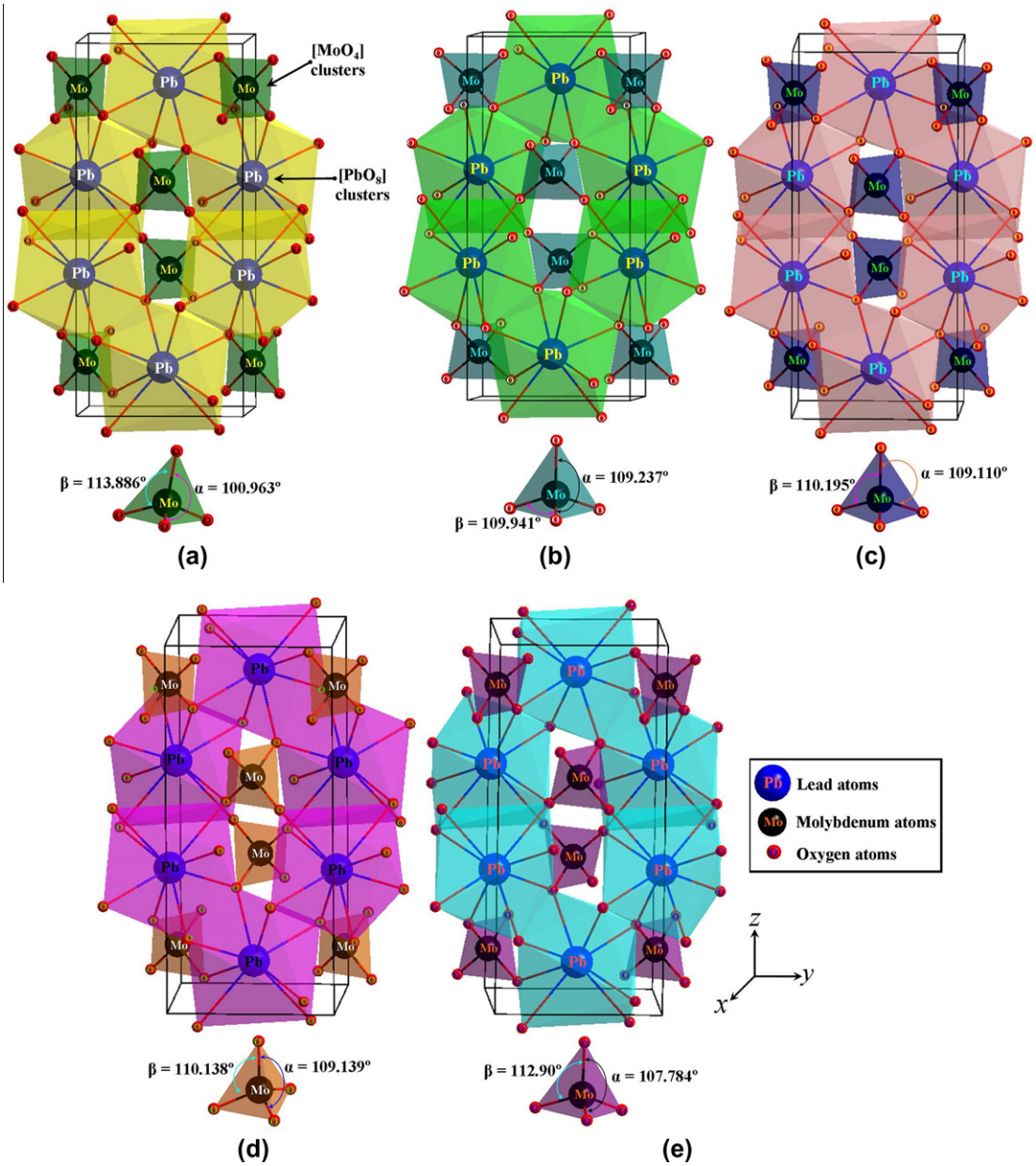

Fig. 2. Schematic representation of PMO ($1 \times 1 \times 1$) unit cells illustrating [PbO_8] and [MoO_4] clusters (α and β) angles between the bonds of O–Mo–O prepared by the: (a) CP method and processed at 70 °C for different times: (b) 2 min, (c) 4 min, (d) 8 min and (e) 10 min in a CH system.

persists in this system due to supersaturated concentrations of chemical acid/salts [98]. Furthermore, a reduction in the quantity of these small PMO crystallites (precipitate) with the crystal growth process was noted. Fig. 5(d) depicts three well faceted PMO crystals as well as other crystals with irregular shapes and holes which may be the result of the dissolution of large crystals and the later recrystallization of (small and large) crystals. An increase in the CH processing time (4 min) raises the collision rate of crystals in the same plane as previously reported for PMO crystals [51]. In this case, the aggregation of crystals (micro-octahedrons) takes place along a common crystallographic path followed by the oriented attachment mechanism [51], where the aggregation of crystals (octahedrons) are interconnected along a common crystallographic orientation (oriented attachment). However, Fig. 5(e) and (f) clearly depicts a predominant growth mechanism for the non-oriented aggregation of crystals. Fig. 5(g) and (h) shows that micro-octahedrons are formed by the aggregation of the first small octahedrons in an oriented manner with a subsequent ripening of the aggregates. Thus, hydrothermal conditions facilitate both the organization and growth of PMO crystals with the Ostwald-ripening mechanism mainly involved when the processing is performed at 70 °C for 8 min. After CH processing performed for 10 min (Fig. 5(i) and (j)), several large PMO crystals are formed by the oriented attachment mechanism based on the spontaneous self-organization of adjacent nanocrystals which results in crystal growth by the coalescence of solid particles that share a common crystallographic orientation [99].

3.6. Average size distribution of $PbMoO_4$ crystals

FE-SEM images were also essential to evaluate the average crystal size distribution of PMO in this study. Hence, the average count of 100 crystals with good quality on the boundary from the FE-SEM images was taken to ensure a good statistical response (Fig. 6(a)–(e)).

After counting the crystals, the Shapiro–Wilk (W) normality test was employed to verify that data are normally distributed and

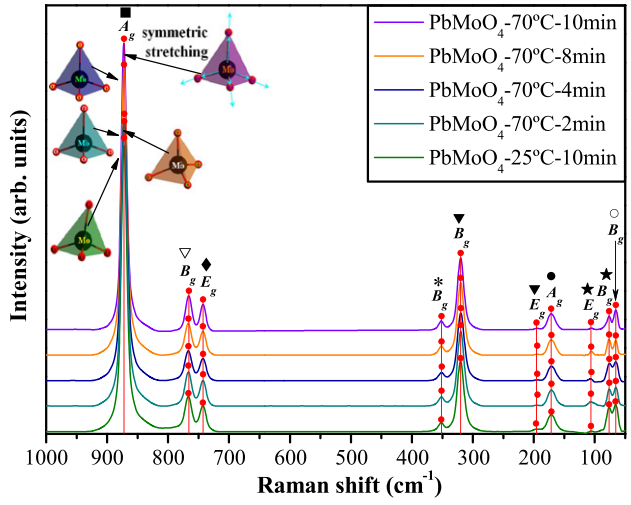

Fig. 3. MR spectra in the range from 1000 to 50 cm^{-1} for PMO crystals prepared by the CP method and processed at 70 °C for different times (from 2 to 10 min) in a CH system. The inset shows the $[MoO_4]$ clusters with a symmetric stretching vibration.

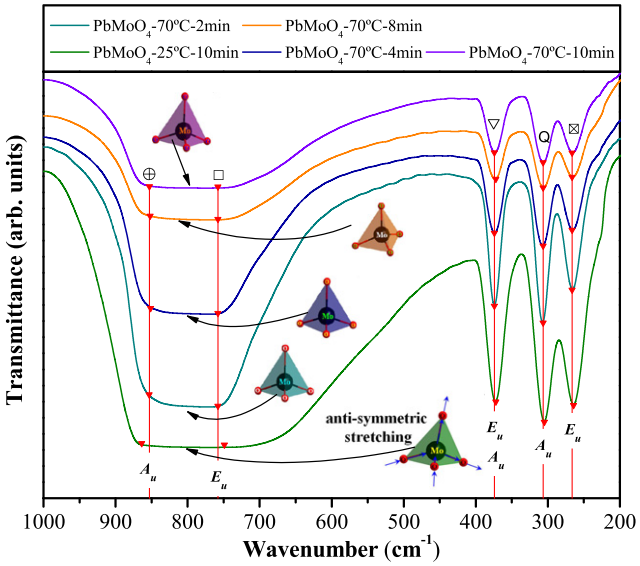

Fig. 4. FT-IR spectra in the range from 1000 to 200 cm^{-1} for the PMO crystals prepared by the CP method and processed at 70 °C for different times (from 2 to 10 min) in a CH system. The inset shows the $[MoO_4]$ clusters with anti-symmetric stretching.

follow a normal distribution [100]. The *W* normality test is useful because other statistical tests (such as the *t*-test) assume that data is sampled from normally distributed crystals. However, a different crystal size can affect the procedures used to test for normality which can be very erratic for small crystals. A *W* statistic and *P* value are computed so a statistical decision can be made by comparison with a level of significance. The *W* statistic is defined as:

$$W = \left(\sum_{i=1}^{n} A_i X_i\right)^2 \Big/ \sum_{i=1}^{n} (X_i - \overline{X})^2 \tag{7}$$

where

$$\overline{X} = \frac{1}{n}\sum_{i=1}^{n} X_i \tag{8}$$

and A_i is a weighting factor. The results for *W* were 0.97556, 0.98168, 0.98168, 0.97556 and 0.97556 for the average crystal size distribution of PMO crystals obtained by the CP method and processed in a CH at 70 °C for 2, 4, 8 and 10 min, respectively. The results for W are all normal at 0.05 level. Therefore, in all cases, the counting of crystal sizes is well-described by a log-normal distribution:

$$y = y_0 + \frac{A}{\sqrt{2\pi}wx} e^{\frac{-[\ln\frac{x_i}{x_c}]^2}{2w^2}}, \tag{9}$$

where y_0 is the first value in the *y*-axis, *A* is the amplitude, *w* is the width, π is a constant and x_c is the center value of the distribution curve in the *x*-axis.

Small octahedron-like PMO crystals obtained by the CP method exhibited an average size distribution in a range from 0.125 to 0.425 μm (Fig. 6(a) and inset). In this system, it is estimated that 26% of these crystals have an average size of approximately 0.225 μm. Fig. 6(b) shows the average crystal distribution in a range from 0.15 to 0.65 μm of PMO crystals processed at 70 °C for 2 min in a CH system (see inset). Approximately 36% of these crystals exhibit an average size of 0.25 μm. As illustrated in Fig. 6(c) and the inset, PMO crystals processed at 70 °C for 4 min have an average size distribution in a range from 0.15 to 0.65 μm, and 34% of these crystals have an average size at around 0.35 μm. Fig. 6(d) and the inset illustrate an average size distribution in a range from 0.25 to 0.85 μm, 25% of PMO crystals have an average size of approximately 0.35 μm. Finally, in Fig. 6(e) and the inset, show the pronounced effect of the crystal growth process where an increase in the average size distribution from 0.3 to 1.5 μm is clearly evident; 33% of crystals processed at 70 °C for 10 min have an average size of around 0.7 μm.

3.7. Growth mechanism of $PbMoO_4$ crystals

Fig. 7(a)–(h) displays the schematic representation of main growth mechanisms involved in the synthesis of PMO crystals by the CP method at room temperature processed at 70 °C for different times (from 2 to 10 min) in a CH system.

Table 3
Comparative results between experimental Raman-active modes for PMO crystals obtained in this study and modes reported in the literature by different synthesis methods.

M	*T* (°C)	*t* (min)	B_g ○	B_g ★	E_g ★	A_g ●	E_g ▼	B_g ▼	B_g *	E_g ◆	B_g ▽	A_g ■	Ref.
CZ	1200	1440	64	75	100	164	190	317	348	744	764	868	[91]
SSR	1300	750	–	–	–	–	–	312	347	742	763	864	[93]
CZ	1250	144	65	78	107	171	193	323	350	748	771	871	[94]
CZ	1000	2880	67	73	103	168	192	317	350	743	760	818	[95]
CP	25	10	66	76	107	171	196	320	352	743	766	872	[✠]
CH	70	2	65	76	106	171	195	320	351	743	766	872	[✠]
CH	70	4	65	76	107	171	195	320	351	743	766	872	[✠]
CH	70	8	65	76	106	171	195	320	351	743	766	872	[✠]
CH	70	10	65	76	107	171	195	320	351	743	766	872	[✠]

M = method; *T* = temperature; *t* = time; Raman modes = (cm^{-1}); CZ = Czochralski; SSR = solid state reactions; CP = coprecipitation; CH = conventional hydrothermal and [✠] = this work.

Table 4
Comparative results between experimental infrared active modes for the PMO crystals obtained in this work and those reported in the literature by different synthesis methods.

M	T (°C)	t (min)	E_u (cm^{-1}) ⊠	A_u (cm^{-1}) ○	E_u (cm^{-1}) ▽	A_u (cm^{-1}) ▽	E_u (cm^{-1}) □	A_u (cm^{-1}) ⊕	Ref.
CZ	1200	1440	270	308	378	378	765	850	[91]
CZ	1100	1440	277	298	367	367	766	868	[95]
SSR	1000	300	–	–	–	–	775	850	[96]
CP	25	10	266	307	374	374	758	853	[✠]
CH	70	2	266	307	372	372	758	852	[✠]
CH	70	4	266	307	374	374	758	851	[✠]
CH	70	8	266	307	374	374	785	853	[✠]
CH	70	10	264	304	373	373	749	864	[✠]

M = method; T = temperature; t = time; infrared modes = (cm^{-1}); CZ = Czochralski; SSR = solid state reactions; CP = coprecipitation; CH = conventional hydrothermal and [✠] = this work.

The initial process for the formation of small octahedron-like PMO crystallites occurs with the addition of stoichiometric amounts of reagents [H_2MoO_4 and $Pb(NO_3)_2$] dissolved in deionized water. In this solution, the solvation energy of the H_2O molecules quickly promotes salt dissociation and acid ionization where Pb^{2+} and MoO_4^{2-} ions are rapidly solvated by H_2O molecules. The partial negative charge on the H_2O molecules is electrostatically attracted by Pb^{2+} ions while the partial positive charge on the H_2O molecules are electrostatically attracted by the MoO_4^{2-} ions [7]. However, due to differences in the electronic density between Pb^{2+} and MoO_4^{2-} ions, a high force strong electrostatic attraction occurs between these ions which results in the formation of the first $PbMoO_{4(s)}$ precipitates or nucleation seeds (Fig. 7(a)). The precipitation rate was then increased by the addition of 5 mL of NH_4OH into this solution to complete the crystallization process (Fig. 7(b)). PMO crystals obtained by the CP method were dried, separated and characterized (Fig. 7(c)). Other syntheses were performed and processed at 70 °C for different times (from 2 to 10 min) in a CH system (Nanox-Technology S/A, NanoxHydrocell H-100, Brazil) [52]. When this suspension was processed at 70 °C for 2 min, an increase occurred in the average PMO crystal size as well as the dissolution process of some crystals in the other suspensions (Fig. 7(d)). Cameirão et al. [97] reported a similar phenomenon for strontium molybdate ($SrMoO_4$) agglomerated crystals. However, without a base (NH_4OH) in this system, much more time was required to check the dissolution process of the $SrMoO_4$ crystals at 70 °C. This behavior takes place when a solid–liquid system is not in equilibrium; i.e., with higher supersaturation, the crystal surface can become rough even if the temperature is lower (a kinetic rough transition) [101]. The FE-SEM images show that PMO crystals processed for 2 min also can undergo the recrystallization process (Figs. 5(c), (d) and 7(d)) which is in agreement with recent research reported in the literature for molybdates [102,103]. An analysis of the results displayed in Figs. 7(e) and 5(e), (f) reveals that PMO crystals have spontaneous self-organization of adjacent particles along a common crystallographic orientation in the [001] direction (Support Information, Fig. SI-5). Therefore, we can conclude that both OA and non-oriented mechanisms co-exist in the crystal growth process. Figs. 7(e) and 5(g), (h) illustrate that most crystals have surface defects, and irregular shapes; thus some PMO crystals follow the OA mechanism. Based on an analysis of FE-SEM images, it is evident that PMO crystals processed for 8 min are formed via a classical growth mechanism; i.e., the OR process (Fig. 7(f)). Thus, the thermodynamically-driven spontaneous process occurs because larger particles are more energetically favored than smaller particles [104]. In this case, both the OR mechanism and oriented coalescence result in anisotropic growth to formation of irregular octahedron-like PMO crystals (Fig. 5(g) and (h)). However, PMO crystals processed for 10 min are predominantly grown by the OA mechanism as well as in the aggregation process (Fig. 7(g)). The OA mechanism due to constant agitation in hydrothermal conditions in aqueous solvents promotes a growth process which controls oriented PMO crystals (Fig. 5(i) and (j)). Fig. 7(h) shows the growth process of PMO crystals with a CH processing time modeled in the KrystalShaper-2010 Version 1.1.6 program [105]. These figures support the proposal of a growth mechanism for these octahedrons growing along the [001] direction since this orientation is the largest distance from the center of the crystal with respect to other crystals (Support Information, Table SI-1).

3.8. UV–Vis absorption spectroscopy analyses of $PbMoO_4$ crystals

UV–Vis spectra of PMO crystals obtained by the CP method and processed at 70 °C for different times (from 2 to 10 min) in a CH system are illustrated in Fig. SI-6(a)–(e), Support Information. Estimated optical band values as a function of CH processing time are shown in Fig. SI-6(f), Support Information.

As illustrated in Fig. SI-6(a)–(e), different E_{gap} values are related to intermediate electronic states. Moreover, we have verified a reduction in E_{gap} values with an increase in CH processing time (Fig. SI-6(f)). In principle, we believe that this behavior is related to an increase in the average crystal size which is mainly due to the formation of new intermediary energy levels within the band gap. Optical band values as a function of CH processing time are presented in Table 5.

Table 5 illustrates that the E_{gap} values for PMO crystals are somewhat different from the values reported by Pandey et al. [106] and Oeder et al. [107]. These discrepancies can be associated with the fact that the E_{gap} is very dependent on the synthetic procedure, different level defects, shape, average crystal size, orientation and distortions in the lattice. However, a comparison of the E_{gap} values obtained in this study and other research reported in the literature are in good agreement [108–110]. This behavior can be related to similar electronic densities or defects into the lattice. In our case, the smaller E_{gap} (3.33 eV) values found for PMO crystals processed at 70 °C for 10 min can be due to the distortion levels in [MoO_4] clusters with angles $\alpha = 112.9^\circ$ and $\beta = 107.784^\circ$ (Fig. 2(e)). Moreover, some defects on the crystal surfaces caused by CH processing can lead to the formation of new intermediary electronic states within the band gap and consequently a reduction in E_{gap} values.

3.9. Photoluminescence analyses: emission spectra of $PbMoO_4$ crystals

Fig. 8 shows PL spectra for PMO crystals while the inset displays digital photos of PL emissions of these crystals during the excitation process by a laser ($\lambda = 350$ nm) at room temperature.

Fig. 8 shows that PMO crystals obtained by the CP method have the PL emission lowest intensity. This behavior can be related to the greatest number of defects in these crystals as verified by FE-SEM images shown in Fig. 5(a) and (b). When PMO crystals

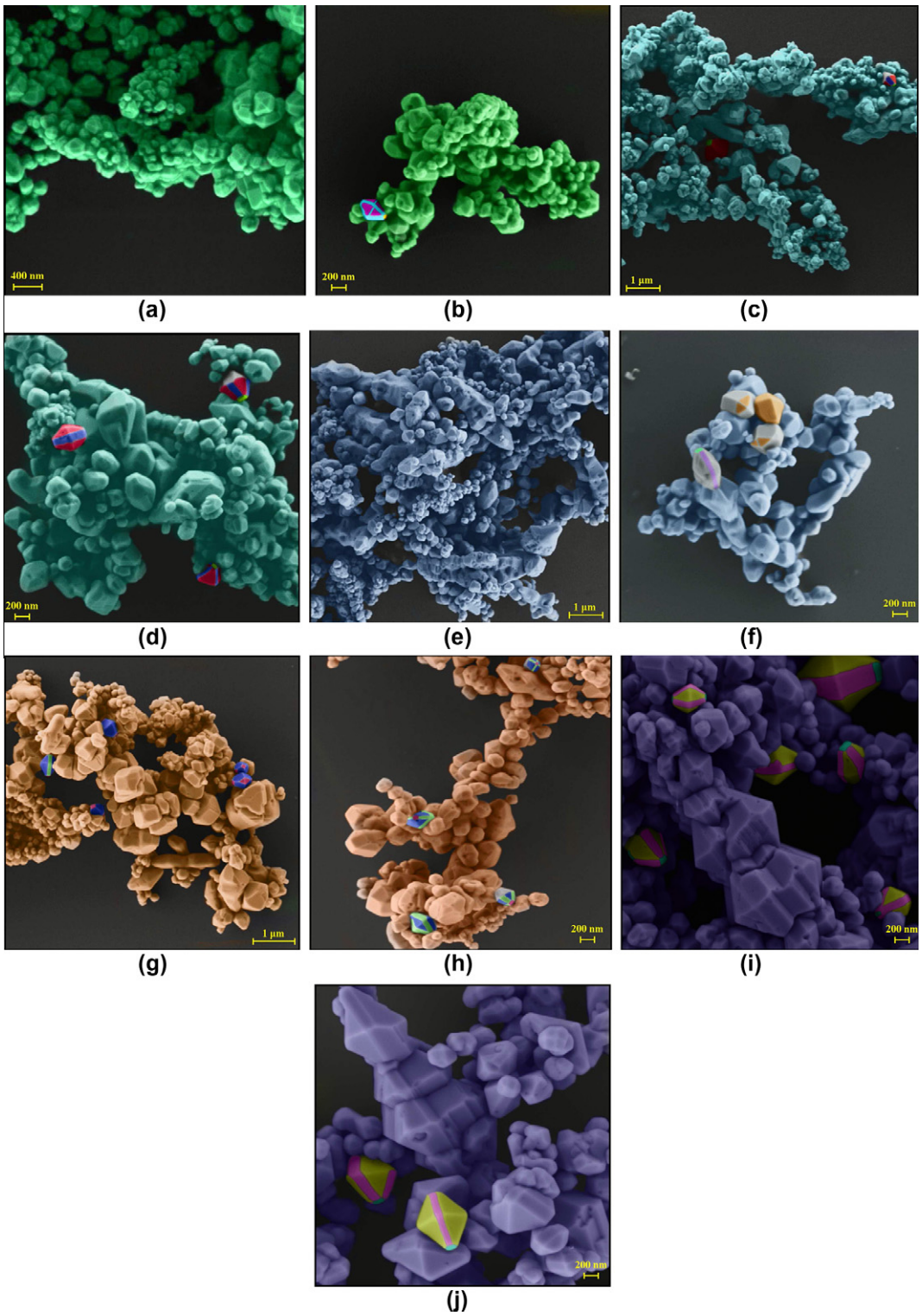

Fig. 5. (a) Low magnification and (b) high magnification FE-SEM images of several PMO crystals prepared by the CP method at room temperature. Highlighted are an individual PMO crystal precipitate (Fig. 5(b)), low magnification and (d) high magnification FE-SEM images of PMO crystals processed at 70 °C for 2 min. Highlighted are five well-faceted PMO crystals (Fig. 5(c) and (d)), (e) low magnification and (f) high magnification FE-SEM images of PMO crystals prepared by the CH method processed at 70 °C for 4 min. Highlighted are several faceted PMO crystals (Fig. 5(f)), (g) low magnification and (h) high magnification FE-SEM images of several PMO crystals (highlighted) processed at 70 °C for 8 min, (i) low magnification and (f) high magnification FE-SEM images of PMO crystals with the OA mechanism processed at 70 °C for 10 min. Highlighted are several well-faceted PMO crystals.

are processed at 70 °C from 2 to 10 min in a CH system, an increase in the PL emission intensity (Fig. 8, Support Information) is evident. In this case, the PL property is improved with a crystal growth process and the possible formation of defects at medium-range. Since a significant peak shift did not occur at maximum PL emission, this characteristic can be attributed to a slight variation in E_{gap} values (3.33–3.40 eV) as discussed previously and shown in Fig. SI-6(a)–(f), Support Information. Moreover, the PL emission of these PMO

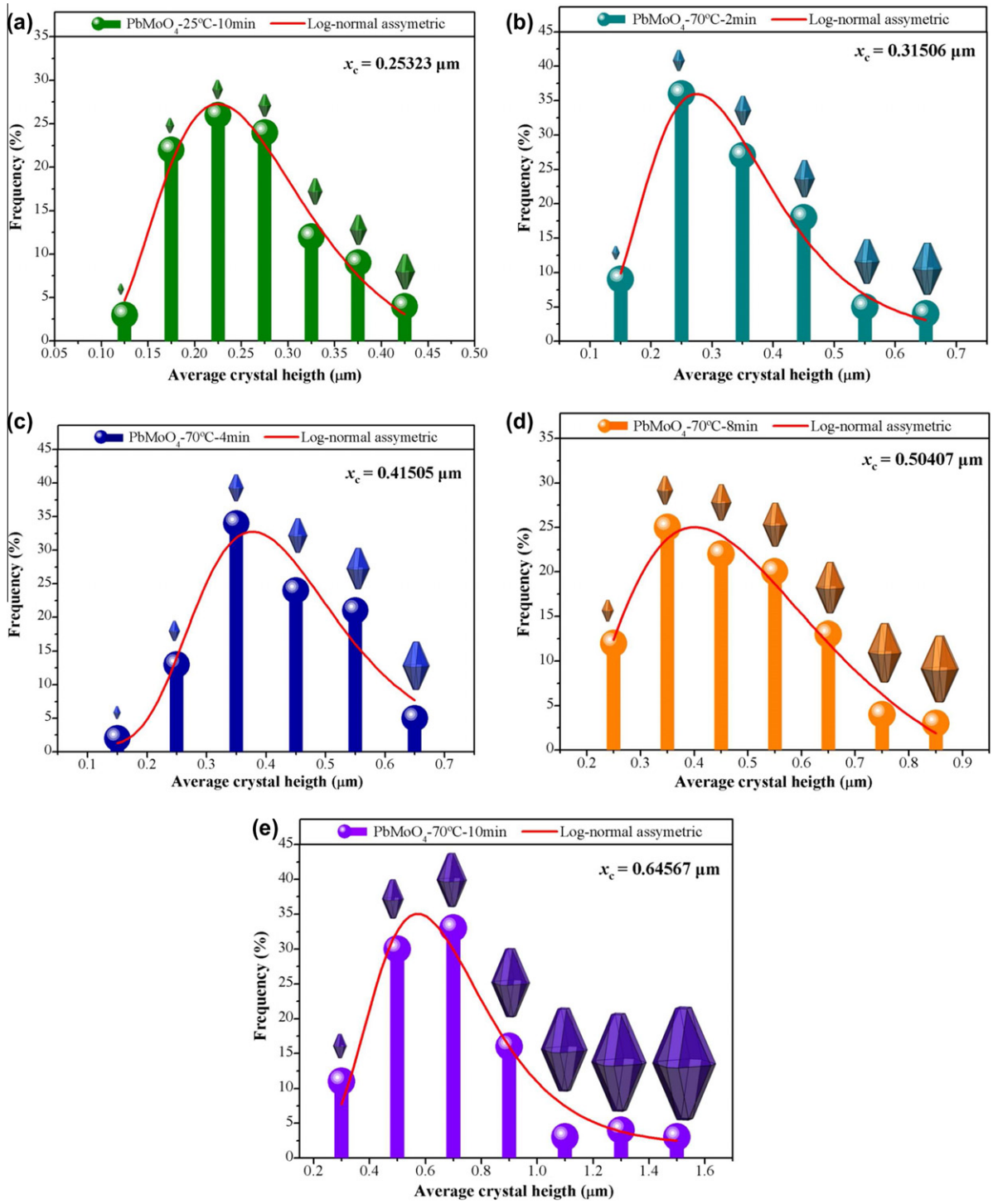

Fig. 6. Average size distribution for PMO crystals prepared by the: (a) CP method and processed at 70 °C for different times: (b) 2 min, (c) 4 min, (d) 8 min and (e) 10 min in a CH system.

crystals was investigated when excited by a laser 406.7 nm (Support Information, Fig. SI-7). PL emission intensity at this wavelength was much lower; with an increase in the PL emission intensity with the raise of the CH processing time produced a similar behavior. Based on the literature [81], this phenomenon will be discussed in detail in the next section using an intermediary energy level (deep and shallow holes) within the band gap. Therefore, our PMO crystals have a larger number of shallow holes in relation to deep holes due to long- and short-range structural disorder (Figs. 2(a) and 3). Therefore, all PMO crystals have highly intense PL emission when excited with energy above the band gap. In recent research [7], our group reported that PL properties are dependent upon distortions in $[MoO_4]$ clusters. These defects/distortions induce a symmetry break in the lattice and lead to the appearance of new intermediate levels within the band gap which are important for a good PL emission at room temperature. Based on this information, our results suggest that the factors, such as: inhomogeneous crystal size distribution, crystallographic orientation of the crystals in a same plane, and surface defects may contribute to improvement of PL properties. We believe that these factors

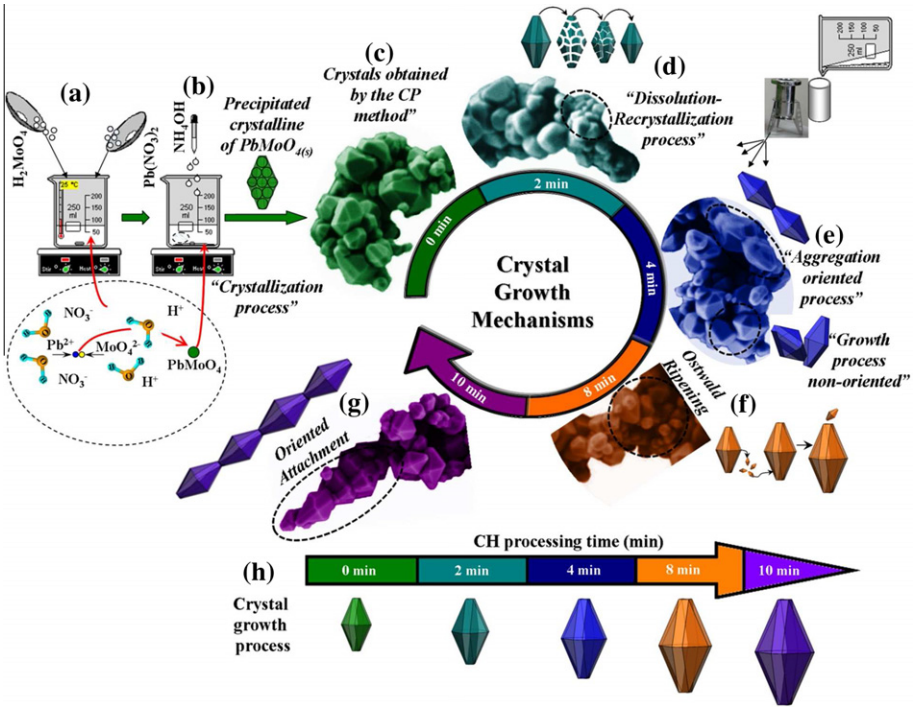

Fig. 7. Schematic representation of the synthesis, processing, and growth mechanisms for PMO crystals by FE-SEM images: (a) chemical synthesis (solvation and CP reactions), (b) increase of precipitation rate with NH_4OH, (c) FE-SEM images for PMO crystals obtained by the CP method and crystallization process, (d) FE-SEM images for PMO crystals processed at 70 °C for 2 min and dissolution–recrystallization process, (e) FE-SEM images for PMO crystals processed at 70 °C for 4 min and growth by the OA non-oriented mechanism, (f) FE-SEM images for PMO crystals processed at 70 °C for 8 min and growth by the OR mechanism, (g) FE-SEM images for PMO crystals processed at 70 °C for 10 min and an OA process and (h) the crystal growth process evolution as a function of CH processing time.

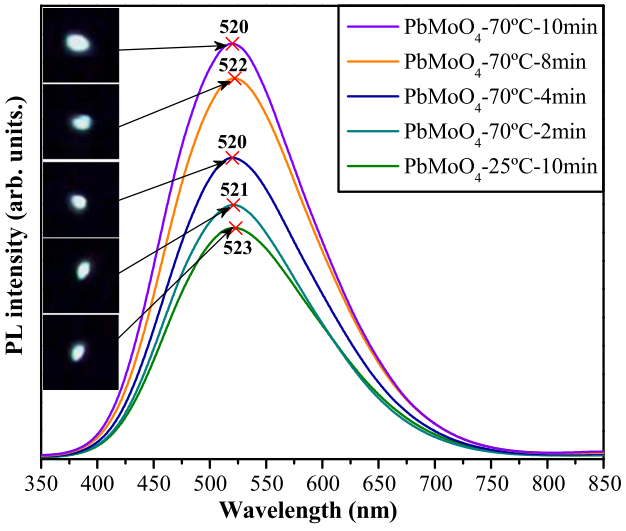

Fig. 8. PL emission spectra for the PMO crystals prepared by the CP method at room temperature and processed at 70 °C for different times (from 2 to 10 min) in a CH system. The inset show the digital photos with the PL emission of PMO crystals.

can be related to the origin of intense PL emission at room temperature in our PMO crystals.

3.10. Wide band model based to explain the photoluminescence properties

To date, few papers in the literature have dealt with the PL properties of pure PMO crystals [51,111–120]. In previous papers, our group reported that the blue PL emission in PMO microcrystals as well as its intensity variations are explained by a model based on both distorted $[MoO_4]$ and $[PbO_8]$ clusters in the lattice [51]. Spassky et al. [111] interpret that the PL emission (band maximum at 490 nm) is generally attributed to radiative transitions in MoO_4^{2-} groups. Nevertheless, these authors also assume that the electronic states of lead in PMO crystals can contribute to an emission center responsible for the luminescence band or can participate in the energy transfer process. Dong and Wu [112] explained that the PL emission (band maximum at 400 nm) in PMO nanobelts can be related to a MoO_4^{2-} groups on the basis of previous reflectivity measurements and the current knowledge of their electronic structure. The top of the valence band with the lowest unoccupied states are composed of the 4*d* states (Mo) split into two sets of bands with *e* (Mo 4*d*) and *t* (O 2*p*) symmetry. Tyagi et al. [113] observed that the green PL emission (band maximum at 490 nm) is dependent upon crystal stoichiometry. Babin et al. [114] assumed that the green PL emission (band maximum at 525 nm) in PMO crystals refers to an excitation in $(MoO_4)^{2-}$ groups. Van Loo

Table 5
Comparative results between the optical band gap energy experimental for the PMO crystals obtained in this study and values reported in the literature by different synthesis methods.

M	Type/shape	*T* (°C)	*t* (min)	E_{gap} (eV)	Ref.
ComP	Powders	–	–	3.2	[106]
CZ	Monocrystal	1000	1440	3.2	[107]
CZ	Monocrystal	1000	2880	3.2	[108]
CP	Octahedron-like	25	10	3.40	[✠]
CH	Octahedron-like	70	2	3.38	[✠]
CH	Octahedron-like	70	4	3.36	[✠]
CH	Octahedron-like	70	8	3.35	[✠]
CH	Octahedron-like	70	10	3.33	[✠]

M = method; *T* = temperature; *t* = time; E_{gap} = Optical band gap; CZ = Czochralski; ComP = commercial powder; CP = coprecipitation; CH = conventional hydrothermal and [✠] = this work.

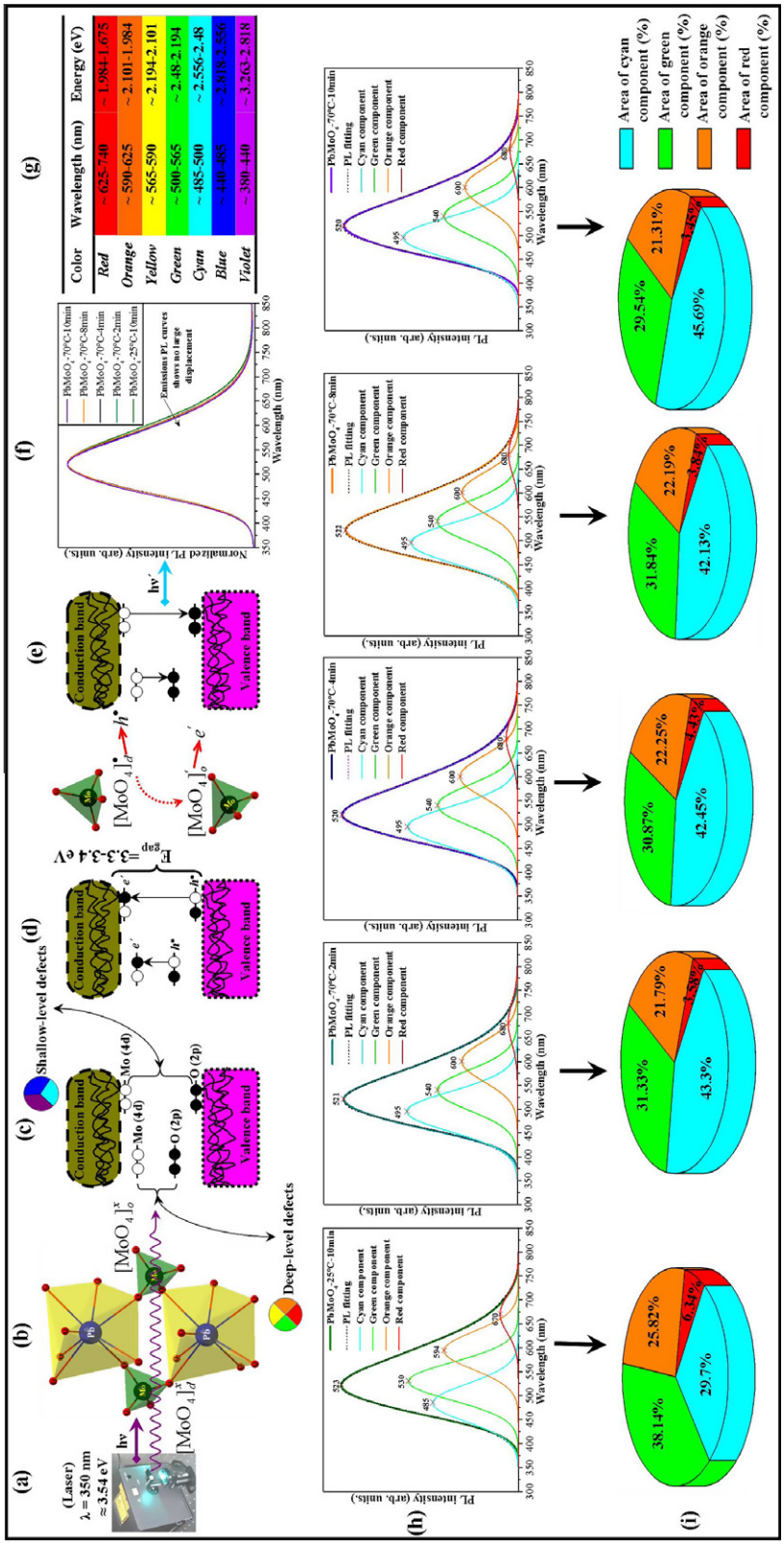

Fig. 9. Model proposed to explain the origin of the intense visible PL emission at room temperature in PMO crystals: (a) wavelength of laser employed in the excitation process of the crystals, (b) presence of a pair (distorted $[MoO_4]^x_d$ and ordered $[MoO_4]^x_o$ clusters) in the lattice which enables a charge transference, (c) proposed wide band model before excitation with intermediary energy levels, (d) electronic transition from oxygen 2*p* orbitals (lower energy levels) to molybdenum 4*d* orbitals (higher energy levels) by absorption of ($h\nu$) at room temperature, (e) emission process of photons ($h\nu'$) due to the radiative return processes of electrons situated at molybdenum 4*d* orbitals to oxygen 2*p* orbitals, (f) normalized PL spectra for PMO crystals prepared by the CP method and processed at 70 °C for different times (from 2 to 10 min) in a CH system, (g) colors of the visible spectrum with its wavelength and energy range, (h) deconvolutions of each normalized PL spectra of PMO crystals and (i) area percentage of each color component corresponding to the emission peak.

[115–117] explained that the blue luminescence in PMO crystals is due to a transition in isolated MoO_4^{2-} groups, and the green-yellow luminescence is due to the superposition of two bands which is caused by the transfer of an electron occupying in orbital with mainly Pb^{2+} ions to an empty orbital of an adjacent MoO_4^{2-} groups with a predominantly *d* character. According to Blasse [118], Groenink and Blasse [119], the PMO crystal PL emission (band maximum at 517 nm) can be assigned to the $^3T_1 \rightarrow {}^1A_1$ transition in the tetrahedral (MoO_4^{2-}) group. It is assumed that the $^3T_1$ level is split due to spin-orbit coupling. In studies of excitation and emission spectra, Bernhardt [120] noted that an orange PL emission (band maximum at 600 nm) in PMO crystals is temperature dependent. Moreover, these authors explained that the fluorescence centers are not identical due to perturbed tetrahedrons in the scheelite structure. Thus, the PL emission process of PMO crystals is not completely understood as yet. As shown above, several authors have tried to explain the origin of this physical property. However, most of these explanations are directly associated with MoO_4^{2-} groups (ions), but PMO is a crystalline solid composed of several units (...[MoO_4]–[PbO_8]–[MoO_4]...) clusters linked among themselves, as previously described and illustrated in Fig. 2(a)–(e).

Therefore, in our study, we assumed the presence of distorted tetrahedral [MoO_4] clusters in the PMO crystal lattice prepared by different CP and CH methods. This affirmation is based on structural refinement data performed for each PMO crystal (Fig. 1(a)–(e) and Table 2). Furthermore, Fig. 2(a)–(e) shows that bonds between the [MoO_4] and [PbO_8] clusters in the tetragonal structure are different due to distortions in the [MoO_4] complex clusters which may promote a slight deformation in the Pb–O bonds (Supporting Information, Fig. SI-4(a)–(e)). Moreover, these distortions are able to induce a symmetry break in the lattice which leads to the appearance of new intermediate levels within the band gap and charge gradient between the clusters which leads to the polarization of the [MoO_4] clusters and consequently in the lattice. We believe that these characteristics have fundamental importance since they promote the formation of intermediate levels which are necessary for probable recombination processes between the distorted/disordered $[MoO_4]_d^x$ complex clusters and ordered $[MoO_4]_o^x$ complex clusters, causes the formation of $[MoO_4]_d^{\bullet}$ and $[MoO_4]_o^{/}$ and/or holes ($h^{\bullet}$) and electrons (e')] which promotes an intense visible PL emission at room temperature in our PMO crystals.

Fig. 9(a)–(i) illustrates a schematic representation of the wide band model to explain the PL emission, with the presence of intermediary energy levels (deep and shallow defects) within the band gap due to the distorted [MoO_4] clusters. In addition, main orbitals belonging to the valence band (VB) and conduction band (CB), PL emission spectra and its deconvolution, as well as the contribution of the different colors in the visible spectrum are depicted.

The wavelength energy used (350 nm ≈ 3.543 eV) is able to excite several electrons localized in different intermediary energy levels within the band gap (Fig. 9(a)). Distorted tetrahedral [MoO_4] clusters possibly promote some distortions in deltahedral [PbO_8] clusters (Fig. 9(b)). This process of symmetry breaking can lead to the formation of intermediary energy levels (deep and shallow defects) within the band gap which are basically composed of O 2*p* orbitals (above the valence band) and Mo 4*d* states (near the conduction band) (Fig. 9(c)). During the excitation process at room temperature, electrons localized at lower intermediary energy levels (O-2*p* orbitals) near the VB absorb photon energies ($h\nu$) at this wavelength. As a consequence of this phenomenon, the energetic electrons are promoted to higher intermediary energy levels (Mo-4*d* orbitals) located near the CB (Fig. 9(d)). When the electrons fall back to lower energy states, again via radiative return processes, the energies arising from this electronic transition are converted to photons ($h\nu'$) (Fig. 9(e)). Fig. 9(f) depicts the normalized maximum PL emission absent in a major shift which agrees with gap values (from 3.33 to 3.40 eV). Fig. 9(g) depicts visible spectrum colors in wavelength (nm) and energy (eV). Fig. 9(h) indicates the results of deconvolution for the normalized PL emission spectra of PMO crystals. An analysis of deconvolution results illustrated in Fig. 9(i) reveal a higher percentage of the red area (6.35%) in PMO crystals prepared by the CP method. An increase in the CH processing time promotes a reduction in value for the red area percentage (3.45–4.45%) with a value increase for the cyan area percentage (29.7–45.69%). This behavior indicates that precipitates PMO crystal have a higher percentage of deep-level defects while PMO crystals processed at 70 °C for different times have a higher percentage of shallow-level defect since these deep-level defects can be linked to components of green–yellow–orange and red colors. On the other hand, shallow-level defects can be linked to components of cyan–blue and violet colors. Moreover, we believe that a set of factors such as size, crystal orientation, shape and surface defects may contribute to intense PL properties for PMO crystals at room temperature.

4. Conclusions

In summary, this paper outlines easy attainment of PMO crystals prepared by CP and CH methods. XRD patterns, Rietveld refinement data and MR spectra indicate that PMO crystals have a scheelite-type tetragonal structure without the presence of deleterious phases. Structural refinement data were employed to model of distorted tetrahedral [MoO_4] clusters using lattice parameters and atomic positions. FT-IR spectra showed vibrational modes related to antisymmetric stretching of [WO_4] clusters. FE-SEM images revealed the agglomerate nature and polydisperse size distribution of PMO crystals. Also, these images indicate an anisotropic growth of PMO crystals by means of the OR and OA mechanisms. Moreover, FE-SEM images were employed to model a preferential growth along the [0 0 1] direction. UV–Vis absorption spectra indicate different optical band gap values which are associated with intermediary energy levels within the band gap. These levels are basically composed of O-2*p* orbitals (above the VB) and Mo-4*d* orbitals (below the CB). A wide band model was used to explain the PL emission of PMO crystals synthesized by the CP method composed by deep-level defects which are associated with green–yellow–orange and red colors. PMO crystals obtained using a CH method for different times produce a higher percentage of shallow-level defects. Finally, the PL properties of PMO crystals are associated to assigned to medium-range shape/crystal, orientation/intrinsic defects on the surface and are mainly due to possible distortions on both distorted tetrahedron [MoO_4] and [PbO_8] clusters in the lattice.

Acknowledgments

The authors thank the financial support of the Brazilian research financing institutions: FAPESP, CNPq, NANOX, CAPES and FAPEPI-GERATEC (No. 01.08.0506.00).

Appendix A. Supplementary data

Supplementary data associated with this article can be found, in the online version, at http://dx.doi.org/10.1016/j.poly.2012.12.001.

References

[1] E.P.N. Damen, D.J. Dieleman, A.F.M. Arts, H.W. de Wijn, Phys. Rev. B 64 (2001) 174303.
[2] J. Bi, L. Wu, Y. Zhang, Z. Li, J. Li, X. Fu, Appl. Catal., B 91 (2009) 135.
[3] R.G. Dickinson, J. Am. Chem. Soc. 42 (1920) 85.
[4] G.G. Zhang, Q.F. Fang, X.P. Wang, Z.G. Yi, J. Phys.: Condens. Matter 15 (2003) 4135.

[5] Y. Shimodaira, H. Kato, H. Kobayashi, A. Kudo, Bull. Chem. Soc. Jpn. 80 (2007) 885.
[6] D.E. Hibbs, C.M. Jury, P. Leverett, I.R. Plimer, P.A. Williams, Mineral. Mag. 64 (2000) 1057.
[7] V.S. Marques, L.S. Cavalcante, J.C. Sczancoski, A.F.P. Alcântara, M.O. Orlandi, E. Moraes, E. Longo, J.A. Varela, M. Siu Li, M.R.M.C. Santos, Cryst. Growth Des. 10 (2010) 4752.
[8] G. Jia, C. Wang, S. Xu, J. Phys. Chem. C 114 (2010) 17905.
[9] C. Lugli, L. Medici, D. Saccardo, Neues Jahrb. Mineral. 1 (1999) 281.
[10] T. Araki, Mem. Coll. Sci. Univ. Kyoto 24 (1957) 155.
[11] L. Vegard, A. Refsum, Nor. Videnskaps-Akad., Oslo. Skrifter, Mat.-Nat. Kl. 2 (1927) 1.
[12] L.G. Sillen, A.L. Nylander, Ark. Kem. Mineral. Geol. (Stockholm) 17A (1943) 4.
[13] D.L. Bish, J.E. Post, Am. Mineral. 78 (1993) 932.
[14] M.L. Moreira, E.C. Paris, G.S. do Nascimento, V.M. Longo, J.R. Sambrano, V.R. Mastelaro, M.I.B. Bernardi, J. Andres, J.A. Varela, E. Longo, Acta Mater. 57 (2009) 5174.
[15] L. Li, Y. Su, G. Li, Appl. Phys. Lett. 90 (2007) 054105.
[16] J.J. De Yoreo, P. Vekilov, Principles of crystal nucleation and growth, in: Biomineralization, Mineralogical Society of America, Washington, DC, 2003, p. 57 (Chapter 3).
[17] L.S. Cavalcante, J.C. Sczancokis, R.L. Tranquilin, J.A. Varela, E. Longo, M.O. Orlandi, Particuology 7 (2009) 353–362.
[18] J. Park, J. Joo, S.G. Kwon, Y. Jang, T. Hyeon, Angew. Chem., Int. Ed. 46 (2007) 4630.
[19] P. Bordui, J. Cryst. Growth 85 (1987) 199.
[20] I. Sunagawa, Crystals: Growth, Morpholohy and Perfection, Cambridge University Press, 2005. p. 20.
[21] H. Cöefen, M. Antonietti, Angew. Chem., Int. Ed. 44 (2005) 5576.
[22] Y. Cheng, Y. Wang, D. Chen, F. Bao, J. Phys. Chem. B 109 (2005) 794.
[23] H. Chu, X. Li, G. Chen, Z. Jin, Y. Zhang, Y. Li, Nano Res. 1 (2008) 213.
[24] V.T. Gabrielyan, O.S. Grunskii, A.A. Gukasov, A.V. Denisov, N.S. Nikogosyan, L.M. Fedorova, Cryst. Rep. 50 (2005) 327.
[25] J. Zheng, F. Huang, S. Yin, Y. Wang, Z. Lin, X. Wu, Y. Zhao, J. Am. Chem. Soc. 132 (2010) 9528.
[26] W. Dong, G. Zhao, B. Song, G. Xu, J. Zhou, G. Han, Cryst. Eng. Comm. 14 (2012) 6990–6997.
[27] R.L. Peen, J.F. Banfield, Science 281 (1998) 969.
[28] C. Ribeiro, E.J.H. Lee, E. Longo, E.R. Leite, Chem. Phys. Chem. 6 (2005) 690.
[29] R.L. Penn, J. Phys. Chem. B 108 (2004) 12707.
[30] J. Zhang, F. Huang, Z. Lin, Nanoscale 2 (2010) 18.
[31] D. Gao, X. Lai, C. Cui, P. Cheng, J. Bi, D. Lin, Thin Solid Films 518 (2010) 3151.
[32] G. Xing, Y. Li, Y. Li, Z. Wu, P. Sun, Y. Wang, C. Zhao, G. Wu, Mater. Chem. Phys. 127 (2011) 465.
[33] X. Wu, J. Du, H. Li, M. Zhang, B. Xi, H. Fan, Y. Zhu, Y. Qian, J. Solid State Chem. 180 (2007) 3288.
[34] Y. Sun, J. Ma, J. Fang, C. Gao, Z. Liu, Ceram. Int. 37 (2011) 683.
[35] L. Ma, Y. Sun, P. Gao, Y. Yin, Z. Qin, B. Zhou, Mater. Lett. 64 (2010) 1235.
[36] Y. Shimodaira, H. Kato, H. Kobayashi, A. Kudo, Bull. Chem. Soc. Jpn. 80 (2007) 885.
[37] S. Lei, X. Peng, X. Li, Z. Liang, Y. Yang, B. Cheng, Y. Xiao, L. Zhou, Mater. Res. Bull. 46 (2011) 601.
[38] W.-S. Wang, L. Zhen, C.-Y. Xu, W.-Z. Shan, Cryst. Growth Des. 9 (2009) 1558.
[39] L. Zhou, W. Wang, H. Xu, S. Sun, Cryst. Growth Des. 8 (2008) 3595.
[40] H. Liu, L. Tan, Ionics 10 (2010) 57.
[41] E.S. Kim, B.S. Chun, R. Freer, R.J. Cernik, J. Eur. Ceram. Soc. 30 (2010) 1731.
[42] G.-K. Choi, J.-R. Kim, S.H. Yoon, K.S. Hong, J. Eur. Ceram. Soc. 27 (2007) 3063.
[43] V.B. Mikhailik, S. Henry, H. Kraus, I. Solskii, Nucl. Instrum. Methods Phys. Res., Sect. A 583 (2007) 350.
[44] I. Bavykina, G. Angloher, D. Hauff, M. Kiefer, F. Petricca, F. Pröbst, Opt. Mater. 31 (2009) 1382.
[45] L. Xu, Y. Zhiping, G. Li, G. Qinglin, H. Sufang, L. Panlai, J. Rare Earths 25 (2007) 706.
[46] C.-J. Mao, J. Geng, X.-C. Wu, J.-J. Zhu, J. Phys. Chem. C 114 (2010) 1982.
[47] D.A. Pinnow, L.G. Van Uitert, A.W. Warner, W.A. Bonner, Appl. Phys. Lett. 15 (1969) 83.
[48] G.A. Coquin, D.A. Pinnow, A.W. Warner, J. Appl. Phys. 42 (1971) 2162.
[49] W.A. Bonner, G.J. Zydzik, J. Cryst. Growth 7 (1970) 65.
[50] A. Vernaleken, M.G. Cohen, H. Metcalf, Opt. Lett. 29 (2007) 7117.
[51] J.C. Sczancoski, M.D.R. Bomio, L.S. Cavalcante, M.R. Joya, P.S. Pizani, J.A. Varela, E. Longo, M. Siu Li, J.A. Andres, J. Phys. Chem. C 113 (2009) 5812.
[52] Available from: <http://www.nanox.com.br/>.
[53] Available from: <http://icsd.fiz-karlsruhe.de.w10001.dotlib.com.br/>.
[54] J.C. Sczancoski, L.S. Cavalcante, M.R. Joya, J.W.M. Espinosa, P.S. Pizani, J.A. Varela, E. Longo, J. Colloid Interface Sci. 330 (2009) 227.
[55] Available from: <http://www.ing.unitn.it/maud/index.html/>.
[56] L. Lutterotti, S. Matthies, H.-R. Wenk, A.J. Schultz, J. Richardson, J. Appl. Phys. 81 (1997) 594.
[57] M. Ferrari, L. Lutterotti, J. Appl. Phys. 76 (1994) 7246.
[58] L. Lutterotti, M. Bortolotti, IUCr Compcomm Newsl. 1 (2003) 43.
[59] L. Lutterotti, S. Matthies, H.-R. Wenk, IUCr Newsl. CPD 21 (1999) 14.
[60] H.M. Rietveld, J. Appl. Crystallogr. 2 (1969) 65.
[61] R.M. Hazen, L.W. Finger, J. Phys. Chem. Solids 46 (1985) 253.
[62] Y. Cheng, Y. Wang, D. Chen, F. Bao, J. Phys. Chem. B 109 (2005) 794.
[63] A. Phuruangrat, T. Thongtem, S. Thongtem, J. Cryst. Growth 311 (2009) 4076.
[64] A. Phuruangrat, T. Thongtem, S. Thongtem, Curr. Appl. Phys. 10 (2009) 342.
[65] G. Will, Powder Diffraction: The Rietveld Method and the Two Stage Method to Determine and Refine Crystal Structures from Powder Diffraction Data, Springer-Verlag, Berlin, Heidelberg, 2006. p. 44.
[66] S.R. Hall, F.H. Allen, I.D. Brown, Acta Crystallogr., Sect. A 47 (1991) 655.
[67] A. Li Bail, J. Non-Cryst. Solids 183 (1995) 39.
[68] L. Lutterotti, M. VoLtoLini, H.-R. Wenk, K. BandyopadHyay, T. Vanorio, Am. Mineral. 95 (2010) 98.
[69] B.F. Mentzen, A. Latrach, J. Bouix, A.W. Hewat, Mater. Res. Bull. 19 (1984) 549.
[70] Available from: <http://www.electrochem.org/dl/ma/206/pdfs/1701.pdf/>.
[71] J. Leciejewicz, Z. Kristallogr. 121 (1965) 158.
[72] Available from: <http://www.crystalimpact.com/diamond/>.
[73] D. Errandonea, D. Santamaria-Perez, V. Grover, S.N. Achary, A.K. Tyagi, J. Appl. Phys. 108 (2010) 073518.
[74] Available from: <http://polyhedra.org/poly/show/0/tetrahedron/>.
[75] Available from: <http://polyhedra.org/poly/show/128/snubdisphenoid/>.
[76] M. Crane, R.L. Frost, P.A. Williams, J.T. Kloprogge, J. Raman Spectrosc. 33 (2002) 62.
[77] D. Christofilos, G.A. Kourouklis, S. Ves, J. Phys. Chem. Solids 56 (1995) 1122.
[78] D.L. Rousseau, R.P. Bauman, S.P.S. Porto, J. Raman Spectrosc. 10 (1981) 253.
[79] J.C. Sczancoski, L.S. Cavalcante, N.L. Marana, R.O. da Silva, R.L. Tranquilin, M.R. Joya, P.S. Pizani, J.A. Varela, J.R. Sambrano, M.S. Li, E. Longo, J. Andrés, Curr. Appl. Phys. 10 (2010) 614.
[80] S.P.S. Porto, J.F. Scott, Phys. Rev. 157 (1967) 716.
[81] T.T. Basiev, A.A. Sobol, Y.K. Voronko, P.G. Zverev, Opt. Mater. 15 (2000) 205.
[82] T.T. Basiev, A.A. Sobol, P.G. Zverev, L.I. Ivleva, V.V. Osiko, R.C. Powell, Opt. Mater. 11 (1999) 307.
[83] G.M. Clark, W.P. Doyle, Spectrochim. Acta 22 (1966) 1441.
[84] A.S. Barker Jr., Phys. Rev. 135 (1964) A742.
[85] A. Golubović, R. Gajić, Z. Dohčević-Mitrović, S. Nikolić, J. Alloys Compd. 415 (2006) 16.
[86] Z.C. Ling, H.R. Xia, D.G. Ran, F.Q. Liu, S.Q. Sun, J.D. Fan, H.J. Zhang, J.Y. Wang, L.L. Yu, Chem. Phys. Lett. 426 (2006) 85.
[87] L.S. Cavalcante, J.C. Sczancoski, R.L. Tranquilin, M.R. Joya, P.S. Pizani, J.A. Varela, E. Longo, J. Phys. Chem. Solids 69 (2008) 2674.
[88] J.C. Sczancoski, L.S. Cavalcante, M.R. Joya, J.A. Varela, P.S. Pizani, E. Longo, Chem. Eng. J. 140 (2008) 632.
[89] T. Thongtem, S. Kungwankunakorn, B. Kuntalue, A. Phuruangrat, S. Thongtem, J. Alloys Compd. 506 (2010) 475.
[90] A.S. Thongtem, V.V. Atuchin, J. Phys. Chem. Solids 71 (2010) 958.
[91] R.K. Khanna, E.R. Lippincott, Spectrochim. Acta 21A (1968) 905.
[92] M. Liegeois-Duyckaerts, P. Tarte, Spectrochim. Acta 28A (1972) 2037.
[93] C. Yu, Q. Yu, C. Gao, B. Liu, A. Hao, C. He, X. Huang, D. Zhang, X. Cui, D. Li, H. Liu, Y. Ma, G. Zou, J. Phys.: Condens. Matter 19 (2007) 425215.
[94] P.G. Zverev, Phys. Status Solidi C 11 (2004) 3101.
[95] V. Musinschi, M. Caraman, C. Musinschi, N. Syrbu, Moldavian J. Phys. Sci. 8 (2009) 186.
[96] H.C. Zeng, J. Mater. Res. 11 (1996) 703.
[97] A. Cameirão, R. David, F. Espitalier, F. Gruy, J. Cryst. Growth 310 (2008) 4152.
[98] A. Magnaldo, M. Masson, R. Champion, Chem. Eng. Sci. 62 (2007) 766.
[99] C.J. Dalmaschio, C.R. Ribeiro, E.R. Leite, Nanoscale 2 (2010) 2336.
[100] S.S. Shapiro, M.B. Wilk, Biometrika 52 (1965) 591.
[101] R.F.P. Grimbergen, H. Meekes, P. Bennema, C.S. Strom, L.J.P. Vogels, Acta Crystallogr., Sect. A 54 (1998) 491.
[102] Y.-S. Luo, W.-D. Zhang, X.-J. Dai, Y. Yang, S.-Y. Fu, J. Phys. Chem. C 113 (2009) 4856.
[103] Z. Luo, H. Li, H. Shu, K. Wang, J. Xia, Y. Yan, Cryst. Growth Des. 8 (2008) 2275.
[104] A.P. Moura, L.S. Cavalcante, J.C. Sczancoski, D.G. Stroppa, E.C. Paris, A.J. Ramirez, J.A. Varela, E. Longo, Adv. Powder Technol. 21 (2010) 197.
[105] Available from: <http://www.jcrystal.com/products/krystalshaper/index.htm/>.
[106] P.K. Pandey, N.S. Bhave, R.B. Kharat, Indian J. Chem., Sect. A 44 (2005) 1186.
[107] R. Oeder, A. Scharmann, D. Schwabe, B. Vitt, J. Cryst. Growth 43 (1978) 537.
[108] A. Kudo, M. Steiberg, A.J. Bard, A. Chmpion, M.A. Fox, T.E. Mallouk, S.E. Webber, J.M. White, Catal. Lett. 5 (1990) 61.
[109] M.D. Volnianskiy, A.Y. Kudzin, S.N. Plyaka, Z.H. Balasmeh, Phys. Status Solidi B 242 (2005) 1349.
[110] Sangeeta, D.G. Desai, A.K. Singh, M. Tyagi, S.C. Sabharwal, J. Cryst. Growth 296 (2006) 81.
[111] D.A. Spasskya, S.N. Ivanov, S.N. Kolobanov, V.V. Mikhailin, V.N. Zemskov, B.I. Zadneprovski, L.I. Potkin, Radiat. Meas. 38 (2004) 607.
[112] F.-Q. Dong, Q.-S. Wu, Appl. Phys. A 91 (2008) 161.
[113] M. Tyagi, Sangeeta, D.G. Desai, S.C. Sabharwal, J. Lumin. 128 (2008) 22.
[114] V. Babin, P. Bohacek, E. Bender, A. Krasnikov, E. Mihokova, M. Nikl, N. Senguttuvan, A. Stolovits, Y. Usuki, S. Zazubovich, Radiat. Meas. 38 (2004) 533.
[115] W. Van Loo, Phys. Status Solidi A 27 (1975) 565.
[116] W. Van Loo, J. Lumin. 10 (1975) 221.
[117] W. Van Loo, Phys. Status Solidi A 28 (1975) 227.
[118] G. Blasse, Struct. Bond. 42 (1980) 1.
[119] J.A. Groenink, G. Blasse, J. Solid State Chem. 32 (1980) 9.
[120] H. Bernhardt, Phys. Status Solid A 91 (1985) 643.